Observations of Water Vapor Mixing Ratio and Flux in Tibetan Plateau

S. Wu[1], G. Dai[1], X. Song[1], B. Liu[1] and L. Liu[2]

[1] {Ocean Remote Sensing Institute, Ocean University of China, Qingdao, China}

[2] {Laboratory of Severe Weather, Chinese Academy of Meteorological Science, Beijing, China}

Corresponding author: S. Wu (wush@ouc.edu.cn)

Abstract

The water vapor ~~expedition experiment~~field campaign was performed~~operated~~ in the Tibetan Plateau in summer ~~during July and August~~ of 2014, by utilizing the ~~Water~~ WAter vapor, Cloud and Aerosol Lidar~~lidar~~ (WACAL). The observation was carried out in Nagqu area (31.5°N, 92.05°E), which is 4508 meters above the mean sea level. During the observation, the water vapor mixing ratio profiles at high elevation were~~was~~ obtained. In this paper, the methodology of the WACAL and the retrieval ~~method~~ are presented in particular. The validation of water vapor mixing ratio measured during the field campaigns is ~~completed~~ performed by comparing the ~~Lidar~~lidar measurements to the radiosonde (RS) data. WACAL observations from July to August illustrate the diurnal variation of water vapor mixing ratio in the planetary boundary layer in this high elevation area. The mean water vapor mixing ratio in Nagqu in July and August is about 9.4 g·kg^{-1} and the values vary from 6.0 to 11.7 g·kg^{-1} near ground. The SNRs and relative errors of the data are analysed and discussed as well in this paper. Finally, by ~~combin~~ concurrent measurements ~~ing~~of the vertical wind speed profiles ~~measured~~ by the coherent wind ~~lidar~~lidar (CDL), the vertical flux of water vapor is calculated ~~and the~~and illustrates the water vapor transport through ~~upwelling~~ updraft and downdraft~~deposition of the water vapor are monitored~~. It is the first application, to our knowledge, to operate continuously atmospheric observation by utilizing multi-disciplinary

~~lidar~~lidars at altitude higher than 4,000 ~~meters~~ meters, which is significant for research on the hydrologic cycle in the atmospheric boundary layer and lower troposphere ~~dynamics and meteorology of~~in the Tibetan Plateau.

1. Introduction

Although the content of water vapor in the atmosphere is very rare and occupies about 0.1%-3% of the content of the atmosphere, water vapor has a significant impact on the determination of weather and climate due to the fundamental role in the radiative energy transfer, hydrological cycle, and atmospheric chemistry processes. It influences the radiative budget of the planet both directly and through coupling with clouds. (Dinoev et al, 2013)~~Through coupling with clouds, water vapor influences the radiative budget of earth both directly and indirectly.~~ Moreover, because of its strong absorption and emission bands, especially in the infrared, water vapor is one of the most significant greenhouse gas. Slight change in the water vapor profile might bring pronounced e~~a~~ffect on the global warming process. It also influences atmospheric circulation and temperature structure by condensation and evaporation processes (Dinoev, 2009). Aiming at the detection of water vapor, the most commonly used method is radiosonde. The humidity sensors in radiosonde, which detect changes in resistance or dielectric constant resulting from absorption or adsorption of water (Wang et al., 2003), are installed. Several inter-comparison studies (Ferrare et al., 1995; Turner and Goldsmith, 1999; Behrendt et al., 2007a, b and Bhawar et al., 2011) have been operated to test the stability of these sensors. As a result, ~~strong~~ systematic differences between different sensors are present for all ranges of humidity and temperature. ~~Consequently, requirement for the new techniques seem to be very significant.~~ ~~Lidar~~~~lidar~~Lidar, as an active remote sensing technique, has the advantage of high temporal and spatial resolution, high-frequency dynamic monitoring. Two ~~Lidar~~lidar (LIght Detect And Ranging) techniques have been applied to the detection of water vapor: the ~~Differential~~ DIfferential Absorption Lidar~~lidar~~ (DIAL) and the Raman ~~Lidar~~lidar technique. In terms of the DIAL, two laser pulses at different wavelengths, called “on-line” and “off-line”, respectively, are emitted to the atmosphere (Browell, 1983; Grant, 1991; Wulfmeyer and

Bösenberg, 1998; Bruneau et al. 2001; Wirth et al., 2009; Vogelmann and Trickl, 2008). In this paper, the ~~Lidar~~lidar system applies Raman technique. This technique was firstly used by Melfi (Melfi et al., 1969 and 1972) and Cooney (Cooney, 1970) and the profiles of water vapor mixing ratio were retrieved and provided. The Raman ~~Lidar~~lidar technique depends on the detection of Raman backscattered radiation from atmospheric molecules (Melfi et al., 1969 and 1972; Renaut and Capitini, 1988). The process of Raman scattering is characterized by a wavelength shift of the scattered radiation in respect to the exciting wavelength. The shift is uniquely associated with the internal transitions between the rotational-vibrational energy levels of the molecules (Inaba and Kobayasi, 1972; Inaba, 1976; Demtröder, 2005 and Demtröder, 2013~~Inaba, 1976; Demtroder, 2005~~), and is used for identification of the scattering molecules. ~~Due to the development~~Because of the advantages of the high power laser source, the vertical ~~operation~~ detection range of the Raman ~~Lidar~~lidars can be extended up to 7km and throughout the troposphere (Whiteman et al., 1992; Vaughan et al., 1988; Goldsmith, 1998; Leblanc et al., 2008; Dinoev 2009 and Dinoev et al. 2013).

The Tibetan Plateau lies at a critical and sensitive junction of four climatic systems: the Westerlies, the East Asian Monsoon, the Siberian cold polar airflow and the Indian monsoon. The Tibetan Plateau is an outstanding topographic feather in the middle of the Eurasian Continent with averaged height above 4500 m (MSL), and has important roles in global and regional climate system. (Kuwagata et al., 2001) ~~In turn, t~~T~~he Tibetan Plateau influences the atmosphere in East Asia area and even the whole northern hemisphere.~~ The Tibetan Plateau has great impact on the water vapor budget of area around. The water vapor transportation based on the plateau-monsoon interaction affects the drought and flood of Asia and even the whole north hemisphere. During the middle of the monsoon season, from the end of June to early September, very intense cloud activity continually exists over the Tibetan Plateau. Even though the altitude is very high, a relatively wet condition is maintained over the Tibetan Plateau and the hydrological cycle is active during the monsoon season (Kuwagata et al., 2001). Consequently, to study the development of water vapor in Tibetan Plateau ~~it is~~becomes the focus of ~~a significant~~ scientific ~~problem~~ concern~~to study the development of water vapor in Tibetan Plateau~~.

~~During the routine observation from 10 July to 16 August, t~~The water vapor mixing ratio is monitored twice one day (00:00 and 12:00 UTC) by the applying of operational radiosondes. However, because of the limitation of the temporal resolution and measurement frequency, the water vapor mixing ratio data from radiosonde cannot satisfy the requirement of nowcast due to the various meteorological situation (Dinoev 2009), especially in the high elevation area with strong radiation and convection. Moreover, the lack of the vertical profiles of water vapor mixing ratio make it difficult to obtain and analyse the vertical distribution of water vapor (Kuwagata et al., 2001). ~~Fortunately, W~~w~~ith the development of the knowledge, some other remote sensing techniques appear. These techniques include passive and active remote sensing.~~ The paper introduces the ~~Lidar~~lidar technique, an active sensing technique, ~~. The Lidar~~lidar ~~is capable of~~to provid~~ing~~e vertical profiles of water vapor mixing ratio with the advantages of high ~~temporal and~~ spatial resolution and updating rate.

Several lidars have been deployed for ~~are developed as~~ mountain-based atmospheric observations~~lidars~~, where~~ and relatively~~ complex ambient conditions resulting from the high altitude above ~~mean~~ sea level ~~are~~ need to be considered~~solved~~. ~~Some special issues regarding the meteorological conditions and problems regarding the ambient conditions at the ground also need be considered.~~ One lidar system was set up and operated in 1973 at the mauna loa observatory (19.53 °N ,155.58 °W, 3400 m mean sea level (MSL)) (DeFoor and Robinson, 1987; DeFoor et al., 1992). This lidar was used for the detection of ~~aerosol and detected~~ the eruption of the Philippine volcano Pinatubo firstly. A combined multiwavelength Raman elastic-backscatter lidar system specially built for measurements in the EARLINET network (Larchevêque et al., 2002). The system was installed in 1999 at the Jungfraujoch Research Station (46.55 °N, 7.98 °E; 3580 m (MSL)) and can monitor the aerosol optical properties and water vapor. In 2003, a powerful ~~differential absorption lidar (~~DIAL~~)~~ at the Schneefernerhaus high altitude station next to the Zugspitze summit (Germany) (Vogelmann and Trickl, 2008; Klanner et al., 2010)~~. This lidar system,~~, –located at 2675 m MSL, provides water vapor profiles in the entire free troposphere above 3 km with high vertical resolution and an accuracy of about 5 % up to 8 km~~ without observable bias~~.

In this paper, the observation of lidars during the ~~third ~~Tibetan Plateau atmospheric expedition experiment campaign is described. The methodology of the water vapor mixing ratio, wind field and vertical water vapor flux ~~is~~are introduced in section 2 and the results and case studies are provided in section 3.

~~During the 2014 Tibetan Plateau atmospheric expedition experiment campaign, the vertical profiles of water vapor mixing ratio are measured by WACAL.~~

2. Lidar technology and ~~Methodology~~methodology

~~During t~~ The 2014 Tibetan Plateau atmospheric expedition experiment campaign was operated in Nagqu (31.5 °N, 92.05 °E, 4508 m MSL) on Tibetan Plateau.~~,~~ During this campaign, the vertical profiles of water vapor mixing ratio ~~are~~were measured by the WACAL and ~~,~~the horizontal and vertical wind ~~field~~profiles ~~is~~were detected by the CDL. Moreover, the temperature, pressure and relative humidity are detected by applying the radiosonde twice one day (00:00 and 12:00 UTC). Combining the data products of the three systems, the water vapor flux can be monitored. In the WACAL system, since the laser chiller inside the cabin generate a lot of heat, which is harmful for the stable operation of the laser, it is essential to cool the air in this cabin. The ventilation facility with high ventilation rate fan ~~is~~was taken into consideration, which plays a very practical role in the high elevation and low air pressure field experiment~~, e.g.~~ at the Tibetan Plateau~~ field campaign~~. ~~Moreover~~In addition, ~~to ensure the normal operation and ~~to avoid the electric arc breaking through the air under the condition of low pressure, ~~reduce the heat of the laser, ~~the rated voltage of ~~the ~~pump lamps in the laser oscillator and amplifiers ~~and oscillator stage is decreased~~were reduced, and therefore the heat load also decreased.

The principle and basic layout of WACAL is described in this section for the integrality and the detailed design is described in a separated paper (Wu et al., 2015). Fig~~ure~~. 1 shows the schematic diagram of WACAL. The laser transmitter of WACAL, Continuum Powerlite 9030, is a high peak power flash lamp pumped Nd:YAG laser with three wavelengths of 354.7 nm, 532 nm and 1064 nm. And the pulse energy is 410 mJ, 120 mJ and 700 mJ, respectively. The flash lamp-pumped Nd:YAG laser transmitter generates light pulses at the wavelength of 1064 nm. And after the second harmonic generator (SHG) and third harmonic generator (THG), the wavelengths of 532 nm (frequency doubled) and 354.7 nm (frequency tripled) are generated. With the residual light at wavelength 1064 nm, all these three beams are transmitted to the atmosphere. The basic parameters are listed in table 3. The light with the wavelength of 354.7 nm is used for exciting Raman backscatter of nitrogen and water vapor molecule. Meanwhile the backscattered light excited by the light at the wavelengths of 532 nm and 1064 nm are utilized for the detection of aerosol and cloud. For purpose of decreasing divergence angle, two beam expanders are designed. As shown in Fig. 1, the transmitter includes laser, one half-wave plate, one reflecting prism, one mirror, two beam expanders and two windows with anti-reflective coating. The expanded laser beams with 90 mm diameter transmit into the atmosphere on an axis closed to the receiver axis.

After a laser pulse is transmitted to the atmosphere, molecules and particles scatter the light in all directions. A portion of the light is scattered backwards to the lidar~~. The light~~ that is collected by telescopes and then transmitted to the detection system. In order to increase the amount of collected light, this system ~~deployed~~uses four Newtonian telescopes with the diameter of 300 mm and the focal length of 1524 mm, forming a telescope array with an equivalent receiver aperture of about 610 mm. The primary mirror of Newtonian telescope is a parabolic mirror while the secondary mirror is a plane mirror. ~~The 4 telescopes assembly served as a telescope array with an equivalent receiver aperture of about 610 mm.~~ The design of the array has better practicability for detecting the signal from near field and far field. Moreover, it takes the collection efficiency of the strong elastic backscatter light and the weak Raman backscatter light into consideration. This design also makes the system easy to transport and suitable for field experiments. However, it makes the system more complicated to align the telescope and to determine the overlap function.

After collected by the telescope array, the scattered light is transmitted into 5 fibers, including 4 far-field fibers and 1 near-field fiber. Considering the overlap function and the collection efficiency of near-field signal, the near-range fiber is designed specially (Wu et al., 2015).

~~The laser at wavelengths of 354.7nm, 532nm and 1064nm are transmitted to the atmosphere after the beam expanders. The diameter of laser at wavelength of 354.7nm is expended from 9mm to 9cm and the divergence angle of the beam is reduced to 0.05mrad. After scattered by the molecular and particles, the backscatter signal is collected by a four-telescope assembly.~~

Here the rotational-vibrational Raman spectrum of nitrogen and water vapor are explained. According to the selection rule for vibrational transitions (Inaba and Kobayasi, 1972; Inaba, 1976; Demtröder, 2005 and Demtröder, 2013), the change of the vibrational quantum number $\Delta\upsilon = 0, \pm 1, \pm 2, \ldots$. However, when come to the area of molecular rotational structure~~atomic fine structure and atomic physics~~, the sublevels cannot be ignored. And the change of the rotational quantum number ΔJ obeys to the transition selection rule $\Delta J = 0, \pm 2$. In turn, the $\Delta\upsilon$ and ΔJ can describe the ~~transitions of the atoms~~rotational resolved molecular transitions. So because of the presence of sublevels, several branches of rotational-vibrational Raman spectrum can be detected as table. 1 shows.

All lines in the Q-branch lie very close to each other and are not resolved excepted with extremely high resolution spectroscopy. The S-branch ($\Delta\upsilon = 1, \Delta J = +2$) and O-branch ($\Delta\upsilon = 1, \Delta J = -2$) are well separated in energy and appear as sidebands on the either side of the Q-branch (Inaba and Kobayasi, 1972). The cross section of nitrogen in Q-branch is about $10^{-30} cm^2 sr^{-1}$, which is two orders of magnitude bigger than the cross section in S- and O-branch (about $10^{-32} cm^2 sr^{-1}$). In table 2, the shift of wave numbers Δk corresponding to $\Delta\upsilon = 1, \Delta J = 0$ of nitrogen and water vapor are listed. In this work~~paper~~, the Q-branch ($\Delta\upsilon = 1, \Delta J = 0$) is applied for the detection. Moreover, by using the narrowband interference filters, the cross-talk of S- and O-branch backscatter light is highly suppressed. ~~The shift of wave number Δk of nitrogen and water vapor are listed in table 2.~~

Since the Raman scattering signal is 2 to 3 orders of magnitude weaker than Rayleigh scattering signal, the detection of the Raman signal at wavelength of 386.7 nm and 407.5 nm is more difficult ~~due to~~because of the much lower SNR. ~~The backscattered laser light is collected by four 304.8 mm in diameter telescopes with focal length of 1524 mm. For the better receiving efficiency and lower height to fit in the compact container,~~ As discussed above, ~~these four telescopes are assembled as~~ a telescope array with~~, and~~ the ~~efficient~~ equivalent aperture of 610 mm.~~receiver widens to 609.6 mm.~~ Four fibers are mounted at the focus of the telescopes for the coupling of the signal. The core diameter of the fiber~~s~~ is 200 microns and the numerical aperture is 0.22, which also serves as a field stop. ~~After~~ Through the coupling of fiber, the Raman signal is delivered to the ~~spectrophotometer~~ spectrometer ~~and~~ which separate~~d as~~ nitrogen Raman signal and water vapor Raman signal. Meanwhile, the ~~532 nm and 1064 nm~~ Mie and Rayleigh scattering signal at 532 nm and 1064 nm are transmitted to the polarization channel and the infrared channel respectively~~. With the help of the polarization channel, the measurements of~~ to retrieve the depolarization ratio, extinction coefficient and ~~clouds~~ cloud height~~are solved~~, which are not described in details in this paper.

The Raman channel is shown in Fig. 1(c). In this figure, the transmitter, receiver and ~~spectrophotometer~~ spectrometer are provided in details. For purpose of avoiding the interference of the elastic backscatter signal, band-pass filters are used. The central wavelength of the filters is 390 nm and the FWHM is 44.6 nm. The transmission between 370 nm and 410 nm is ~~bigger~~ greater than 93% and the optical density (OD) is ~~bigger~~ greater than 5 for light at the wavelength of 354.7 nm and 532 nm. ~~After the filters, four fibers are mounted for the coupling of the signal. After the coupling of fiber, the Raman signal is delivered to the spectrophotometer and separated as Raman signal of nitrogen and water vapor.~~

When the signal is transmitted to ~~spectrophotometer~~the spectrometer, the light is dispersed and then collimated by the convex lens with the focal length of 50.0 mm. After the reflection of the reflecting prism, the parallel light arrives at the grating. The groove density of the grating is 1302 l/mm and the blaze is 400 nm. ~~So far, t~~The Raman scattering signal from~~of~~ nitrogen and water vapor ~~are~~ separate~~d~~ and go in different directions to the photomultiplier tubes (PMT) because of the grating diffraction. Then the additional narrow band filters are used before the PMT to suppress the interference from the elastic scattering and the stray light~~ensure the purity of each signal at 386.7nm and 407.5nm~~. The central wavelengths (CWLs) ~~of the filter-1 is~~ are 407.5 $\pm$ 0.1nm~~. Meanwhile, the CWLs are~~, 386.7 $\pm$ 0.1 nm and 354.7 $\pm$ 0.08 nm for filter-1, filter-2 and filter-3, respectively. The FWHM of all filters is 0.5 $\pm$ 0.10 nm and the peak transmittance is ~~bigger~~ greater than 50% and OD is 5 when out of band blocking from 200 to 1200 nm. Note that together with the filters ~~before~~at the incident end of the fibers, the total OD in the Raman channel is >10 to eliminate the interference from the elastic backscatter signal. After the filtration of filters, the ~~parallel~~ scattering signals are~~is~~ then focused by plano-convex lens with a focal length of 100mm. Finally, the signals are acquired by the ~~photomultiplier tubes which~~PMTs, which are mounted at the focal point of plano-convex lens. The specifications of the optical elements of this channel are shown in table.3.

The ~~Lidar~~Raman lidar equation can be described as Eq. (1) (Dinoev, 2009):

$$P(z,\lambda_R) - P_{BG} = P_0(\lambda_L)\Delta z \frac{A_0 O(z)}{z^2} \xi(\lambda_R) \beta_R^{\pi}(z,\lambda_R) T^{up}(z,\lambda_L) T^{down}(z,\lambda_R) \tag{1}$$

$$\begin{aligned} T^{up}(z,\lambda_L) &= \exp[-\int_{z_0}^{z} \alpha(z',\lambda_L) dz'] \\ T^{down}(z,\lambda_R) &= \exp[-\int_{z}^{z_0} \alpha(z',\lambda_R) dz'] \end{aligned} \tag{2}$$

Where $P_0(\lambda_L)$ is the laser pulse energy at a wavelength of λ_L, P_{BG} is the background signal and noise, Δz is the range resolution, A_0 is the aperture of the telescope, $O(z)$ is the overlap of the system at height of z, $\xi(\lambda_R)$ is the receiving efficiency at a given wavelength λ_R, $\beta_R^{\pi}(z,\lambda_R)$ is the backscatter coefficient at λ_R at an altitude of z, $\alpha(z,\lambda_L)$ and $\alpha(z,\lambda_R)$ are~~is~~ the extinction coefficient at wavelengths of λ_L and λ_R~~,~~ respectively. $T^{up}(z,\lambda_L)$ and $T^{down}(z,\lambda_R)$ are the atmospheric transmission at λ_L and λ_R respectively.

According to Eq. (1), the backscatter signal of N_2 and H_2O are obtained as $P(z,\lambda_{N_2})$ and $P(z,\lambda_{H_2O})$. The water vapor mixing ratio can be calculated by Eq. (3):

$$w(z)=C\frac{P(z,\lambda_{H_2O})}{P(z,\lambda_{N_2})}\Delta T(\lambda_{N_2},\lambda_{H_2O},z) \tag{3}$$

Where: C is the calibration constant and can be obtained by contrast of ~~Lidar~~lidar data and radiosonde data, $\Delta T(\lambda_{N_2},\lambda_{H_2O},z)$~~–~~, contributed by molecular and aerosol extinction, is the differential atmospheric transmission at nitrogen and water vapor Raman wavelengths and is calculated by Eq. (4):

$$\Delta T(\lambda_{N_2},\lambda_{H_2O},z)=\exp\left(-\int_{z_0}^{z}[\alpha(z',\lambda_{N_2})-\alpha(z',\lambda_{H_2O})]dz'\right) \tag{4}$$

The $\alpha(z',\lambda_{N_2})$ and $\alpha(z',\lambda_{H_2O})$ can be calculated by Raman method (Ansmann et al., 1992). The calibration constant is retrieved using linear regression to a vertical water vapor mixing ratio profile obtained by a reference radiosonde of GTS1 type. The radiosonde provides temperature accuracy of $\pm 0.2\,^{\circ}C$, relative humidity accuracy of $\pm 5\%$ and pressure accuracy of $\pm 1\,hPa$. ~~The calibration constant is retrieved using regression to a vertical water vapor mixing ratio profile obtained by a reference radiosonde. The radiosonde provides temperature profiles with measurement accuracy of 2 %.~~ Additionally, the pressure and relative humidity profiles are also obtained. The Eq. (5) is used to obtain a mixing ratio profile from radiosonde data. In this equation, the temperature, pressure and relative humidity profiles are used and the mixing ratio WR (g/kg) is then estimated.

$$WR = \varphi * S = \varphi * \frac{0.622 * P_s(T)}{P - 0.378 * P_s(T)} \tag{5}$$

Where: φ is the relative humidity, S is the specific humidity, P is the atmospheric pressure and P_s is the saturated vapor pressure (mb) at temperature T ($^\circ C$) and can be calculated by Arden-Buck equation (Buck, 1981) as Eq. (6) shows:

$$P_s(T) = 6.1121 \times \exp((18.678 - \frac{T}{234.5}) \times (\frac{T}{257.14 + T})) \tag{6}$$

~~Where: φ is relative humidity, P is the pressure and P_s is the saturated vapor pressure at temperature T and can be calculated by Eq. (6):~~

The calibration constant for this comparison was ~~retrieved using regression to a vertical water vapor mixing ratio profile obtained by a reference radiosonde~~~~was obtained by regressing the lidar~~lidar ~~profile (up to 5 km) to radiosonde~~ as shown in Fig. 2. The ~~lidar~~lidar water vapor mixing ratio (W_{Lidar}) profile ~~was~~ is calculated according to Eq. (3) with a calibration constant set to one. We assume that the relationship between ~~Lidar~~lidar data $W_{Lidar} = \Delta T(\lambda_{N_2}, \lambda_{H_2O}, z) * P(z, \lambda_{H_2O}) / P(z, \lambda_{N_2})$ and radiosonde data W_{Sonde} as Eq. (7):

$$W_{Sonde} = C * W_{Lidar} + D \tag{7}$$

Where C is the calibration constant and D is the offset. Before the field campaign in the Tibetan Plateau, the water vapor profiles of the WACAL were compared with the measurements of radiosonde at the campus of Ocean University of China in Qingdao. Since the radiosondes were launched every day at 00:00 and 12:00 UTC, the ~~Lidar~~lidar measurements covered the period for the purpose of validation. The radiosondes were launched at the site of Meteorological Administration of Qingdao (36.07 °N,120.33 °E) ~~everyday~~, while the WACAL was deployed at Ocean University of China (36.165 °N,120.4956 °E). As Fig. 2(a) shows, the distance between these two sites is 16.7 km. In table 4, the period of time of the simultaneous observations by radiosonde and WACAL is provided.

Using the linear regression model, the lidar and radiosonde profiles are fitted. The slope ~~from~~using the linear regression fitting~~ the fit~~ is a direct estimation of the lidar calibration constant C. According to Fig. 2(b), C is found to be equal to 219. D is the offset and determined as -0.34. Result from the different observation stations of the WACAL and radiosonde and the WACAL system error, the offset exists. The correlation coefficient of measurements by ~~these~~ two systems is 0.83. The standard deviation is 1.4 and the number of samples is 169. After the calibration the water vapor mixing ratio can be rewritten as Eq. (8)~~the lidarlidar and radiosonde profiles are fitted. The slope C from the fit is a direct estimation of the lidarlidar calibration constant, and is found to be equal to 219. Meanwhile, the D is determined as 0.34. As Fig. 2 shows, the correlation coefficient of these two system data can reach up to 0.83. The standard deviation is 1.4 and the number of samples is 169. After the calibration the water vapor mixing ratio can be rewritten as Eq. (8):~~

$$W_{Lidar}^{Cal} = 219 * W_{Lidar} - 0.34 \tag{8}$$

3. Observation ~~consequences~~ results and discussion

Atmospheric observations were ~~operated~~ performed in the Tibetan Plateau ~~during~~ from 10 July ~~and~~ to 16 August, 2014 by utilizing the WACAL and other lidars. The Tibetan Plateau atmospheric expedition experiment campaign had been carried out in Nagqu (31.5 °N, 92.05 °E), which is 4508 meters above the mean sea level.

In ~~our system~~the WACAL, both of Analog-to-Digital ~~AD~~ (AD~~Analog-to-Digital~~) signal and Photon Counting ~~PC~~ (PC~~ Photon Counting~~) signal are detected by the ~~photomultiplier tube (~~PMTs~~)~~. However, Data acquisition by the PC method is possible only when the photons are individually distinguishable (Whiteman et al., 1992). In other words, because of the saturation effect and the bandwidth limitation of PMTs, the response of counting system is nonlinear. As a result, we have to correct Nitrogen and ~~Oxygen~~ water vapor ~~echo~~ scattering signal by the equation next:

$$P_{real} = \frac{P_{meas}}{1-\tau * P_{meas}} \qquad (\cancel{7}9)$$

Where P_{real} is the actual number of photons detected by PMTs, P_{meas} is the measured ~~number~~ counts and τ is the resolving time of the discriminator counter combination of PMTs, which is also known as the dead-time. After the correction, the actual signal of nitrogen and water vapor Raman signal will be draw in Fig. 3.

~~Aiming at the validation of~~ In order to validate the calibration equation, the scatter diagram ~~based on the~~of the measurements by calibrated ~~Lidar~~lidar method~~data~~ and radiosonde ~~data measured~~ in Nagqu is ~~drawn~~ shown as Fig. 4~~:~~.

Note that~~According to the figure above~~~~Fig. 4,~~ the correlation coefficient can ~~reach~~ be up to 93.54% and mean deviation is 0.77 g•kg^{-1}. As a conclusion, the calibration of ~~the water vapor mixing ratio~~ WACAL measurement can give a reasonably accurate estimate of water vapor profile ~~is accurate enough~~ for the routine observation. Here we ~~will~~ provide some case studies in Fig. 5 for the discussion. Several inter-comparisons of ~~Lidar~~lidar derived vertical profiles with radiosonde measurements are presented (Fig. 5) as well as time serials~~series~~ of water vapor mixing ratio in Nagqu from July 10 to August 16, 2014 (Fig. 6).

In Fig. 5, the blue dashed line indicates the water vapor mixing ratio measured by ~~Lidar~~lidar and the ~~pink~~ horizontal line shows the error bar of the data. Meanwhile the red line shows the data which are ~~gotten~~ obtained from the operational radiosonde. From these four figures, one dry layer ~~could~~ can be seen at about 2.8 km to 3 km in figure (a) and one distinct wet layer ~~could~~ can be ~~seen~~ found at about 1.5 km to 2 km in figure (c). And in ~~figure~~ Fig. 5 (b) and (d), the water vapor mixing ratio gradually decreased as height increase. All of the water vapor mixing ratio profiles is averaged every 60 minutes and the range resolution is 75 m.

The Tibetan Plateau not only feed the most of Asia's major rivers, it also holds scattered numerous lakes. ~~Note that~~ Nagqu is located in the ~~inland~~ north central part of the Tibetan Plateau that is a sub-frigid, semi-arid, monsoon climate zone, with the largest lake, Nam Co Lake, in Tibet in the southeast.~~area,~~ The average annual precipitation is 380 - 420 mm, 80%

of which is in summer and autumn. The~~the~~ content of water vapor in Nagqu is abundant in summer because of the monsoon activities and ~~. It is likely that this phenomenon may result from the abundant vegetation, precipitation and~~ strong evaporation from nearby plateau lakes ~~in July and August~~.

~~However, since the nitrogen concentration at altitude of 4508 meters is about 42% lower than at sea level altitude, the density and the backscatter coefficient of water vapor is also lower in Nagqu. Consequently, the measurement Signal-to-Noise-Ratio (SNR) is getting smaller and the error bar is bigger.~~

According to the profiles of water vapor mixing ratio, the observation ~~data~~ results of the ~~Lidar~~lidar and operational radiosonde have a good consistency. ~~However, the divergence cannot be ignored.~~ Since the nitrogen concentration at elevation of 4508 meters is about 42% lower than that at sea level, the density and the backscatter coefficient of water vapor is also much lower in Nagqu with high elevation over 4500 m. Furthermore, because~~Since~~ the background light in Nagqu was still strong at 20:00 LST (LST=UTC+8) and the strong solar radiation in ultra violet is caused by shallow atmosphere~~,~~, it also brought in errors~~is difficult to~~ in ~~measure~~ the water vapor mixing ratio measurement~~accurately by WACAL~~. ~~For~~ To ~~ensuring~~ ensure the accuracy of the measurement, the WACAL ~~was utilized~~measured the water vapor profiles from 21:30 LST, which is 1.5h later than the measurement of radiosonde. The measuring time difference may be the main error source of observation in Nagqu.

In Fig. 6, the water vapor mixing ratio measured by the WACAL and the radiosonde are presented. The time serials of water vapor mixing ratio from these two systems are provided in Fig. 6(a) and (c) respectively. And the trend of W_{Lidar}^{Cal} is shown and two dry or low water vapor content time periods are found. Fig. 6(b) and (d) provides the mean water vapor mixing ratio and the deviation measured by WACAL and radiosonde. The deviation of water vapor mixing ratio from WACAL and radiosonde which is shown in Fig. 6(e) indicates that the water vapor mixing ratio measured by WACAL is about 0.7 g•kg^{-1} smaller than that measured by radiosonde. This result is also consistent with the mean deviation from Fig. 4 and can also explain the different of water vapor mixing ratio between Fig. 6(a) and (c). ~~Here the time~~

~~serials of water vapor mixing ratio profile at 13:30 UTC from July, 10 to August 16 is shown in Fig. 6. The trend and variation of the water vapor during this summer field observation can be distinctly illustrated. According to Fig. 6(a), the trend of W_{Lidar}^{Cal} was getting smaller with the development of the time in July and August which might result from the gradually withered vegetation. In July, the vegetation is abundant in Nagqu. And maybe because of the transpiration of plants, water vapor content is rich. However, in August, the wilt of vegetation may lead to the decrease of water vapor content.~~

In the following section, the error of the signal and results are discussed. For the purpose of ~~determining~~ evaluating detection performance of the ~~Lidar~~lidar system, the SNR is taken into consideration~~. The SNR~~, which can be described as Eq. (~~8~~10) (Papayannis et al., 1990; Pelon and Mégie, 1982):

$$SNR_i = \frac{P_i}{\sqrt{P_i + P_{bi}}} \tag{~~8~~10}$$

Where P_i is the backscatter signal, P_{bi} is the solar background signal.

Moreover, from Eq. (3), the relative error δ_{RE} can also be calculated by Eq. (~~9~~11):

$$\delta_{RE} = \frac{1}{\sqrt{N}}\left(\frac{1}{SNR_1{}^2} + \frac{1}{SNR_2{}^2}\right) \tag{~~9~~11}$$

Where N is the number of profiles used for averaging. SNR_1 and SNR_2 are the signal to noise ratio of nitrogen and water vapor respectively.

Here we will present one case study of the SNR and δ_{RE} in the following figure.

In Fig. 7, the SNR and relative error are analyzed. Because of the limitation of the lower water vapor content, the acceptable detection range is 3.5 km. The ~~biggest~~ greatest SNR for nitrogen and water vapor in this observation are 6.8 and 0.22, respectively.

According to Fig. 5 and Fig. 6, it is noted that the water vapor mixing ratio are several times higher than the global average, and still at least two times higher than in a tropical atmosphere at corresponding altitudes. ~~For the explanation, t~~The backward trajectory model HYSPLIT (Draxler and Rolph, 2003; Rolph, 2003) from NOAA is ~~taken into account~~used to analyze the possible sources of the water vapor. Corresponding to Fig. 5, four backward trajectories ending at 21:00LST on 11, 15, 18 and 22 July 2014 simulated by HYSPLIT model are provided ~~(Draxler and Rolph, 2003; Rolph, 2003)~~in Fig. 8. The black star represents the observation station of lidar in Nagqu. On the basis of the trajectories, the high water vapor ~~mixing ratio~~content ~~maybe~~ partly resulted from ~~the input~~the advection ~~of the air mass~~ from the Southeast Asian warm pool region. ~~And~~Furthermore, ~~–~~according to our observation by the CDL, the east wind dominates the wind field during the field experi~~e~~ments in Nagqu ~~area~~, which may indicate the influence of the Asian monsoon. As a conclusion, ~~perhaps~~ the observed high water vapor mixing ratio is likely effected by the combination of the ~~moist air mass~~moisture from Southeast Asian warm pool region and Asian monsoon.

In addition to the water vapor content measurements, ~~During the experiment campaign, for purpose of detection the flux of water vapor,~~ the wind ~~field~~ profiles ~~is~~were ~~–~~ also measured by ~~utilizing~~ a compact CDL~~Coherent Doppler Lidarlidar~~ developed by the OUC ~~lidar~~lidar group to calculate the water vapor flux. The ~~Coherent Doppler lidarlidar~~CDL takes advantage of the fact that the frequency of the echo signal is shifted compared to the local-oscillator light because of the Doppler ~~affect~~ effect which occurs from backscattering of aerosols. The details of the CDL system is described in a separated paper (Wu et al. 2014). The Doppler shift in the frequency of the backscattered signal is analyzed to calculate the line-of-sight (LOS) velocity component of the air motion. The Doppler shift f_D can be obtained by Eq. (~~10~~12):

$$f_D = \frac{2|\vec{V}_{LOS}|}{\lambda} \qquad (\cancel{10}12)$$

Where $\vec{V}_{LOS}$ is the line-of-sight (LOS) velocity, λ is the laser wavelength and is equal to 1550 nm in this ~~lidar~~lidar system.~~–~~

When the LOS velocities in four directions $\vec{V}_{LOS,E}$, $\vec{V}_{LOS,W}$, $\vec{V}_{LOS,S}$ and $\vec{V}_{LOS,N}$ are measured, the vertical wind speed can be calculated by Eq. (~~11~~13) (Cariou, 2011):

$$\vec{V}_{ver} = \frac{1}{4\sin\theta}(\vec{V}_{LOS,E} + \vec{V}_{LOS,W} + \vec{V}_{LOS,S} + \vec{V}_{LOS,N}) \qquad (\cancel{11}13)$$

Where θ is the elevation angle.

~~Since water vapor mixing ratio is the most common unit in boundary layer meteorology, it is used to describe the water vapor measurements throughout the work.~~ With the ~~synchronized~~concurrent observations of the water mixing ratio and vertical velocity, the vertical water vapor flux $Flux_{WV,ver}$ can be calculated by Eq. (~~12~~14) (Giez et al., 1999):

$$Flux_{WV,ver}(T) = \overline{W^{Cal}_{Lidar} * \left|\vec{V}_{ver}\right|} \qquad (\cancel{12}14)$$

~~Where ρ_{WV} is the absolute humidity that can be obtained from the water vapor mixing ratio.~~

Where W^{Cal}_{Lidar} and $\vec{V}_{ver}$ are the time serials of the turbulent fluctuations in the water vapor mixing ratio and the vertical wind speed. The bar represents the temporal average over the time interval T. For the consistency of the symbols, the symbols in Eq. (14) are different from the original paper (Giez et al., 1999).

Although the water vapor mixing ratio can only be measured in the nighttime in this field experiment, ~~Result from the unique atmospheric characteristics and heating power of the Tibetan Plateau~~ ~~the~~a longtime serials observation of vertical wind velocity is still important to be required to recognize the unique atmospheric characteristics and heating power over the Tibetan Plateau.~~.~~ From th~~is~~e wind observation, the turbulence, updraft and downdraft at different time period in one day can be detected and analyzed. ~~For this purpose, one~~One case study on 15 July 2015 is provided in Fig. 9. ~~During~~From 0000 LST ~~and~~to 0927 LST, because of the low temperature and rare human and industrial activities, the boundary layer in Tibetan plateau is too~~very~~ low ~~and cannot~~ to be detected by the CDL with a ~~detection blind region~~minimum detection limit of ~~60~~90 m. During the daytime, the turbulence can be found and the value of the vertical wind velocity is between ± 1 $m \cdot s^{-1}$. However, the turbulence in nighttime is rare and the vertical wind velocity is between 0 $m \cdot s^{-1}$ and 1 $m \cdot s^{-1}$, which indicates that the ~~upwelling~~updraft of the atmosphere ~~on the Tibetan Plateau~~due to the difference in temperature between the heated ground and the cooled air in nighttime.

In term of the vertical velocity and vertical water vapor flux, one case study on 15 August 2014 is presented below. Figure 10(a) shows the time serials of range correction backscattering signal measured by the WACAL and ~~Figure~~Fig ~~8~~10(~~a~~c) is the time serials of the vertical velocity profile of 164 minutes obtained from the CDL~~Coherent Doppler Wind Lidar~~lidar. ~~By combining~~ the ~~absolute humidity~~~~water vapor mixing ratio (Fig. 8~~10~~(b)) and vertical wind velocity data, the~~ Then we can calculate the vertical water vapor flux from the water vapor mixing ratio (Fig. 10(b)) and the vertical wind velocity ~~can be calculated and the temporal development is shown in~~ (Fig. ~~9~~11). The temporal resolution (Δt) and the spatial resolution (Δr) of the vertical wind velocity is 22 s and 13 m respectively. And the original Δt and Δr of the water vapor mixing ratio is 10 min and 3.75 m respectively. However, in order to ~~sample~~capture the turbulent processes, the simultaneous observations of the WACAL and CDL should have ~~with~~ the same sampling rate and the high resolution~~and same and by WACAL and CDL are required~~. ~~For this purpose~~Therefore, the Δt and Δr of WACAL are adjusted to be equal to those of the CDL by means of interpolation and moving average.

~~Vertical profiles~~The time serials of water vapor mixing ratio shown in Fig. ~~8~~10(b) indicates that the water vapor ~~mixing ratio~~content inside clouds which are located at the height of 1.0 km to 1.5 km at time period from 21:40 LST to 22:25 LST is 8.63 $\pm$ 1.66 $g{\bullet}kg^{-1}$, higher than that in the ambient atmosphere ~~around~~. ~~The water vapor mixing ratio in the cloud is around 8.631.66 .~~ It can be found ~~According to~~in Fig 10(a) that~~,~~ it started to rain at about 22:00 LST. ~~From these figures, i~~It's also worth mentioning that~~t is noted that~~ the water vapor ~~kept~~ transported ~~rising~~~~upwelling and depositing~~both by the updraft and downdraft and the flux ~~is~~was about 1.20 $\pm$ 2.48 $g{\bullet}kg^{-1}{\bullet}m{\bullet}s^{-1}$ ~~during~~ between 21:03 and 22:00 LST before the rain~~ing~~. Meanwhile, in the process of rain~~ing~~, the water vapor inside the clouds kept transporting downwards ~~depositing~~ and the flux is about -3.37 $\pm$ 2.24 $g{\bullet}kg^{-1}{\bullet}m{\bullet}s^{-1}$. Note that because of the coverage ~~and blocking~~ of ~~the~~ raindrops~~ gathered~~ on the optical windows of

WACAL, the water vapor mixing ratio measured ~~during the time period of~~between 22:05 LST and~~to~~ 22:10 LST ~~should be used carefully and is~~were removed by data quality control.~~during the calculation of the flux.~~ ~~Consequently~~Nevertheless, a small-scale water vapor cycling can be recognized~~was formed partly~~, in which~~ and~~ the ascending and descending~~upwelling and deposition~~ of the water vapor were monitored.

4. Summary

In this study, we have presented atmospheric observations during the Tibetan Plateau atmospheric expedition experiment campaign in 2014 in Nagqu. With the help of the WACAL, we observed the ~~atmosphere~~ water vapor profiles in Tibetan Plateau and obtained information about the atmospheric conditions. The key findings of ~~our~~ this study are listed below.

1) The calibration and validation of water vapor mixing ratio measurement have been completed. In the process of the calibration, we found a ~~the~~ correlation coefficient ~~reached~~ of ~~up to~~ 0.91~~.34%~~ between the measurements of lidar and radiosondes. ~~And in t~~The ~~process of the~~ validation~~,~~ experiment shows a~~the~~ correlation coefficient ~~is~~ of 0.~~93~~94~~.54%~~ and the standard deviation ~~is~~ of 0.77 g•kg^{-1}. Considering the ~~space~~ distance and measurement time difference between the ~~Lidar~~lidar ~~system~~ and radiosondes, the deviation is acceptable~~.~~, indicating that the lidar as a useful remote sensing tool can be used for high temporal and spatial monitoring of water vapor profile.

~~2) With WACAL, significant information about water vapor is acquired.~~ Water vapor mixing ratio profile in ~~Nagqu~~ the Tibetan Plateau is measured for the first time to our knowledge and ~~the~~ some case studies are provided in this paper.

~~3)~~2) The observations were operated in Nagqu from July to August, 2014~~.~~ And the water vapor content in Tibetan plateau ~~during July and August~~in summer was ~~rich~~relatively high~~.~~, mainly because the monsoon activities dominated and the abundant moisture evaporated from nearby constellation plateau lakes. ~~To a certain extent, this phenomenon maybe results from the abundant vegetation, precipitation, evaporation from near plateau lakes effect. Aand perhaps t~~The moist air from the Southeast Asian warm pool region ~~is~~maybe another ~~significant~~ source of the water vapor~~.~~. ~~And~~ A~~a~~ccording to the ~~our~~wind observation by the coherent Doppler lidar~~CDL~~, the east wind dominated~~s~~ ~~the wind field~~in summer in Nagqu area, ~~which may~~ indicating~~e~~ the influence of the Asian monsoon. ~~the wet East Asian Monsoon and the Indian monsoon, water vapor content in Tibetan plateau during July and August was rich.~~

~~4)~~3) According to the ~~diurnal variation~~time serials of water vapor mixing ratio at 21:30 LST from July, 10 to August 16, the development~~trend~~ of water vapor mixing ratio ~~W^{Cal}_{Lidar}~~ was ~~getting smaller with the development of the time in July and August~~monitored~~provided~~ and two dry or low water vapor content cases~~time periods~~ were~~are~~ found.

~~5)~~4) ~~With the help of~~ Using multi-functional lidar techniques of Doppler wind lidar and Raman lidar~~the WACAL and the Coherent Doppler Wind Lidar~~lidar, the vertical wind speed and vertical water vapor flux ~~are~~ can be calculated~~.~~ So as to monitoring t~~T~~he ascending and descending ~~upwelling and deposition~~ of the water vapor~~–~~ in a synoptic process.~~are monitored~~.

Acknowledgements

We thanks our colleagues for their kindly support before and during the field experiment, including Kailin Zhang from Ocean University of China (OUC) for preparing the hardware and conducting the lidar transportation; Xiaochun Zhai and Dongxiang Wang for operating lidars in Nagqu; Rongzhong Li and Xitao Wang from Seaglet Environment Technology for maintaining the Doppler lidar; Zhiqun Hu from Chinese Academy of Meteorological Science for the coordinating of field experiments; Jianhua Ye from Genuine Optronics Limited for his kindly supplying the backup circuit of the laser. This work was partly supported by the National Natural Science Foundation of China (NSFC) under grant 41375016, 41471309 and

91337103, by the China Special Fund for Meteorological Research in the Public Interest under grant GYHY201406001.~~ The authors wish to thank Dr. Liping Liu from CAMS/LAWS for his help and support before and during the observations. Thanks to the whole Lidar~~lidar ~~group of Ocean University of China (OUC).~~ The authors gratefully acknowledge the NOAA Air Resources Laboratory (ARL) for the provision of the HYSPLIT transport and dispersion model and/or READY website (http://www.ready.noaa.gov) used in this publication.

References

Ansmann, A., Wandinger, U., Riebesell, M., Weitkamp, C., and Michaelis, W.: Independent measurement of extinction and backscatter profiles in cirrus clouds by using a combined Raman elastic-backscatter lidar, Appl. Opt., 31, 7113-7131, 1992.

Behrendt, A., Wulfmeyer, V., Bauer, H.-S., Schaberl, T., Di Girolamo, P., Summa, D., Kiemle, C., Ehret, G., Whiteman, D. N., and Demoz, B. B.: Intercomparison of water vapor data measured with lidar during IHOP_2002. Part I: Airborne to ground-based lidar systems and comparisons with chilled-mirror hygrometer radiosondes, J. Atmos. Oceanic Tech., 24, 3-21, 2007a.

Behrendt, A., Wulfmeyer, V., Schaberl, T., Bauer, H.-S., Kiemle, C., Ehret, G., Flamant, C., Kooi, S., Ismail, S., and Ferrare, R.: Intercomparison of water vapor data measured with lidar during IHOP_2002. Part II: Airborne-to-airborne systems, J. Atmos. Oceanic Tech., 24, 22-39, 2007b.

Bhawar, R., Di Girolamo, P., Summa, D., Flamant, C., Althausen, D., Behrendt, A., Kiemle, C., Bosser, P., Cacciani, M., and Champollion, C.: The water vapour intercomparison effort in the framework of the Convective and Orographically - induced Precipitation Study: airborne - to - ground - based and airborne - to - airborne lidar systems, Q. J. R. Meteorol. Soc., 137, 325-348, 2011.

Browell, E. V.: Remote sensing of tropospheric gases and aerosols with an airborne DIAL system. In: Optical and laser remote sensing, Springer, Berlin Heidelberg, 138-147, 1983.

Bruneau, D., Quaglia, P., Flamant, C., Meissonnier, M., and Pelon, J.: Airborne ~~lidar~~lidar LEANDRE II for water-vapor profiling in the troposphere. I. System description, Appl. Opt., 40, 3450-3461, 2001.

Buck, A. L.: New equations for computing vapor pressure and enhancement factor, J. Appl. Meteorol., 20, 1527-1532, 1981.

Cariou, J. and Boquet, M.: LEOSPHERE pulsed ~~lidar~~lidar principles, Leosphere, Orsay (FR), 2011. 1-32, 2011.

Cooney, J.: Remote measurements of atmospheric water vapor profiles using the Raman component of laser backscatter, J. Appl. Meteorol., 9, 182-184, 1970.

DeFoor, T. and Robinson, E.: Stratospheric lidar profiles from Mauna Loa Observatory, winter 1985 - 1986, Geophys. Res. Lett., 14, 618-621, 1987.

DeFoor, T. E., Robinson, E., and Ryan, S.: Early lidar observations of the June 1991 Pinatubo eruption plume at Mauna Loa Observatory, Hawaii, Geophys. Res. Lett., 19, 187-190, 1992.

Demtröder, W.~~Demtroder, W.~~: Molecular physics: theoretical principles and experimental methods, Wiley VCH, Weinheim, 2005.

Demtröder, W.: Laser spectroscopy: basic concepts and instrumentation, Springer Science & Business Media, 2013.

Dinoev, T.: Automated Raman ~~lidar~~lidar for day and night operational observation of tropospheric water vapor for meteorological applications, 2009. ÉCOLE POLYTECHNIQUE FÉDÉRALE DE LAUSANNE, 2009.

Dinoev, T., Simeonov, V., Arshinov, Y., Bobrovnikov, S., Ristori, P., Calpini, B., Parlange, M., and Van den Bergh, H.: Raman Lidar for Meteorological Observations, RALMO-Part 1: Instrument description, Atmos. Meas. Tech., 6, 1329-1346, 2013.

Draxler, R. R. and Rolph, G.: HYSPLIT (HYbrid Single-Particle Lagrangian Integrated

Trajectory) model access via NOAA ARL READY website (http://www. arl. noaa. gov/ready/hysplit4. html). NOAA Air Resources Laboratory, Silver Spring. Md, 2003.

Ferrare, R., Melfi, S., Whiteman, D., Evans, K., Schmidlin, F., and Starr, D. O. C.: A comparison of water vapor measurements made by Raman ~~lidar~~lidar and radiosondes, J. Atm. Ocean. Tech., 12, 1177-1195, 1995.

Giez, A., Ehret, G., Schwiesow, R. L., Davis, K. J., and Lenschow, D. H.: Water vapor flux measurements from ground-based vertically pointed water vapor differential absorption and Doppler lidars, J. Atmos. Oceanic Tech., 16, 237-250, 1999.

Goldsmith, J., Blair, F. H., Bisson, S. E., and Turner, D. D.: Turn-key Raman ~~lidar~~lidar for profiling atmospheric water vapor, clouds, and aerosols, Appl. Opt., 37, 4979-4990, 1998.

Grant, W. B.: Differential absorption and Raman ~~lidar~~lidar for water vapor profile measurements: a review, Opt. Eng., 30, 40-48, 1991.

Inaba, H. and Kobayasi, T.: Laser-Raman radar—Laser-Raman scattering methods for remote detection and analysis of atmospheric pollution, Opto-electron., 4, 101-123, 1972.

Inaba, H.: Detection of atoms and molecules by Raman scattering and resonance fluorescence. In: Laser monitoring of the atmosphere, Springer, Berlin Heidelberg, 153-236, 1976.

Klanner, L., Trickl, T., and Vogelmann, H.: Combined Raman lidar and DIAL sounding of water vapour and temperature at the NDACC station Zugspitze, 15414, 2010.

Kuwagata, T., Numaguti, A., and Endo, N.: Diurnal variation of water vapor over the central Tibetan Plateau during summer, J. Meteorol. Soc. Jpn., 2, 79, 401-418, 2001.

Larchevêque, G., Balin, I., Nessler, R., Quaglia, P., Simeonov, V., van den Bergh, H., and Calpini, B.: Development of a multiwavelength aerosol and water-vapor lidar at the Jungfraujoch Alpine Station (3580 m above sea level) in Switzerland, Appl. Opt., 41, 2781-2790, 2002.

Leblanc, T., McDermid, I. S., and Aspey, R. A.: First-year operation of a new water vapor

Raman lidar at the JPL Table Mountain Facility, California, J. Atmos. Oceanic Tech., 25, 1454-1462, 2008.

Melfi, S., Lawrence Jr, J., and McCormick, M.: Observation of Raman scattering by water vapor in the atmosphere, Appl. Phys. Lett., 15, 295-297, 1969.

Melfi, S.: Remote measurements of the atmosphere using Raman scattering, Appl. Opt., 11, 1605-1610, 1972.

Papayannis, A., Ancellet, G., Pelon, J., and Megie, G.: Multiwavelength ~~lidar~~lidar for ozone measurements in the troposphere and the lower stratosphere, Appl. Opt., 29, 467-476, 1990.

Pelon, J. and Mégie, G.: Ozone monitoring in the troposphere and lower stratosphere: Evaluation and operation of a ground‐based ~~lidar~~lidar station, J. Geophys. Res., 87, 4947-4955, 1982.

Renaut, D. and Capitini, R.: Boundary-layer water vapor probing with a solar-blind Raman ~~lidar~~lidar: validations, meteorological observations and prospects, J. Atmos. Oceanic Tech., 5, 585-601, 1988.

Rolph, G.: Real-time Environmental Applications and Display sYstem (READY) Website (http://www. arl. noaa. gov/ready/hysplit4. html). NOAA Air Resources Laboratory, Silver Spring, Md, 2003.

Turner, D. D. and Goldsmith J. E. M.: 24-hour Raman ~~lidar~~lidar water vapor measurements during the Atmospheric Radiation Measurement program's 1996 and 1997 water vapor intensive observation periods, J. Atmos. Oceanic Tech., 16,1062–1076, 1999.

Vaughan, G., Wareing, D., Thomas, L., and Mitev, V.: Humidity measurements in the free troposphere using Raman backscatter, Q. J. R. Meteorol. Soc., 114, 1471-1484, 1988.

Vogelmann, H. and Trickl, T.: Wide-range sounding of free-tropospheric water vapor with a differential-absorption lidar (DIAL) at a high-altitude station, Appl. Opt., 47, 2116-2132, 2008.

Wang, J., Carlson, D. J., Parsons, D. B., Hock, T. F., Lauritsen, D., Cole, H. L., Beierle, K., and Chamberlain, E.: Performance of operational radiosonde humidity sensors in direct comparison with a chilled mirror dew‐point hygrometer and its climate implication, Geophys. Res. Lett., 30, 16, 2003.

Whiteman, D., Melfi, S., and Ferrare, R.: Raman ~~lidar~~lidar system for the measurement of water vapor and aerosols in the Earth’s atmosphere, Appl. Opt., 31, 3068-3082, 1992.

Wirth, M., Fix, A., Mahnke, P., Schwarzer, H., Schrandt, F., and Ehret, G.: The airborne multi-wavelength water vapor differential absorption lidar WALES: system design and performance, Appl. Phys. B, 96, 201-213, 2009.

Wu, S., Yin, J., Liu, B., Liu, J., Li, R., Wang, X., Feng, C., Zhuang, Q., and Zhang, K.: Characterization of turbulent wake of wind turbine by coherent Doppler lidar, 2014, 92620H-92620H-92610.

Wu, S., Song, X., Liu, B., Dai, G., Liu, J., Zhang, K., Qin, S., Hua, D., Gao, F., and Liu, L.: Mobile multi-wavelength polarization Raman lidar for water vapor, cloud and aerosol measurement, Opt. Express, 23, 33870-33892, 2015.

Wulfmeyer, V. and Bösenberg, J.: Ground-based differential absorption ~~lidar~~lidar for water-vapor profiling: assessment of accuracy, resolution, and meteorological applications, Appl. Opt., 37, 3825-3844, 1998.

Table 1 Branches of the rotational-vibrational Raman spectrum

$\Delta\upsilon$	ΔJ	Branch
$\pm1,\pm2$	-2	O-branch
$\pm1,\pm2$	0	Q-branch
$\pm1,\pm2$	+2	S-branch

Table 2 The shift of wave number of nitrogen and water vapor

Molecule	Excitation wavelength	Δk $\Delta\upsilon=1,$ $\Delta J=0$	The center of the Q-branch
Nitrogen	354.7nm	2330.7 /cm	386.7nm
Water vapor	354.7nm	3651.7 /cm	407.5nm

Table 3 System specification of the Raman channel of the ~~LidarLidar system~~WACAL

System	Specification	
Laser	Wavelength (nm)	~~355~~354.7
	Pulse energy (mJ)	410
	Repetition rate (Hz)	30
	Divergence (mrad)	0.5
	Pulse width (ns)	3-7
	Stability (±%)	4.0
Beam expender	Amplification factor	×10 @ 355 nm
Telescope	Aperture (mm)	304.8
	Focal length (mm)	1524
Fiber	Aperture (μm)	200

Polychromator	Collimating Lens	Focal length:50mm
	Grating	D: 1302 l/mm Blaze: 400nm
	Filter-1	CWL: 407.5±0.1nm, FWHM :0.5±0.10nm Peak %T: 50%, OD5
	Filter-2	CWL: 386.7±0.1nm, FWHM: 0.5±0.10nm Peak %T: 50%, OD5
	Filter-3	CWL=354.7nm±0.08nm, FWHM: 0.5 ±0.10nm Peak %T: 50%, OD5
	Lens	Focal length:100mm
Photomultiplier tube (Hamamatsu H10721P-110)	Photocathode Area Size (Dia. mm)	0.8
	Cathode radiant sensitivity	~100mA•W^{-1} @ 355 nm
	Wavelength (Peak, nm)	400
Data acquisition system (~~Licel~~ Licel transient recorder)	Temporal resolution (ns)	25
	Range resolution (m)	3.75
	Maximum counting rate (MHz)	250

Table 4 Period of time of the simultaneous observations

May, 2014	12	21	22	26	27	28	29	31
June, 2014	3	4	5	6	7	8	9	10

	12	14	15	16	17	18	20	23

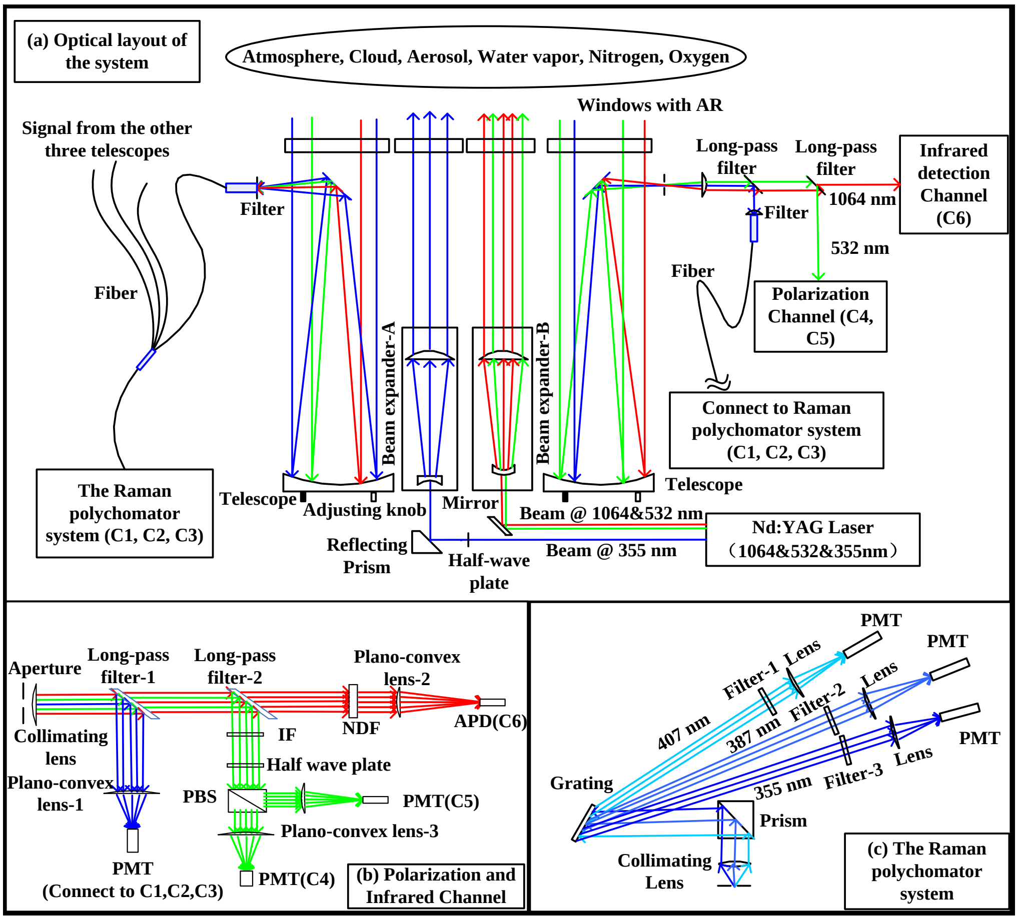

Fig. 1 Schematic diagram and photos of WACAL

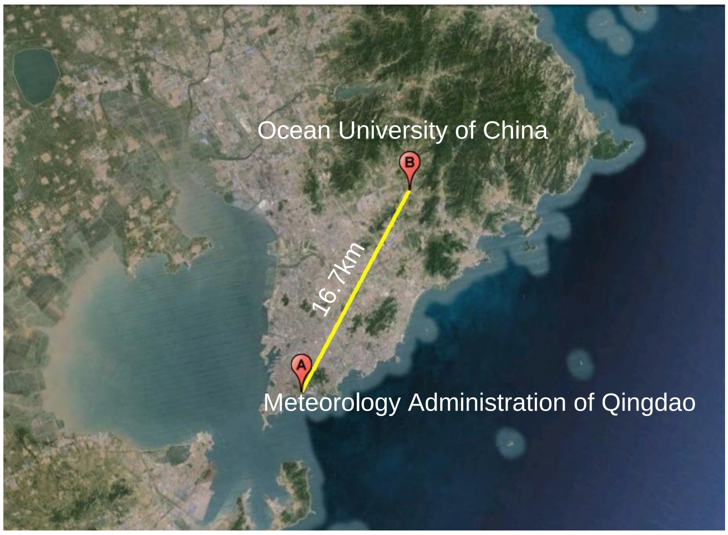

(a)

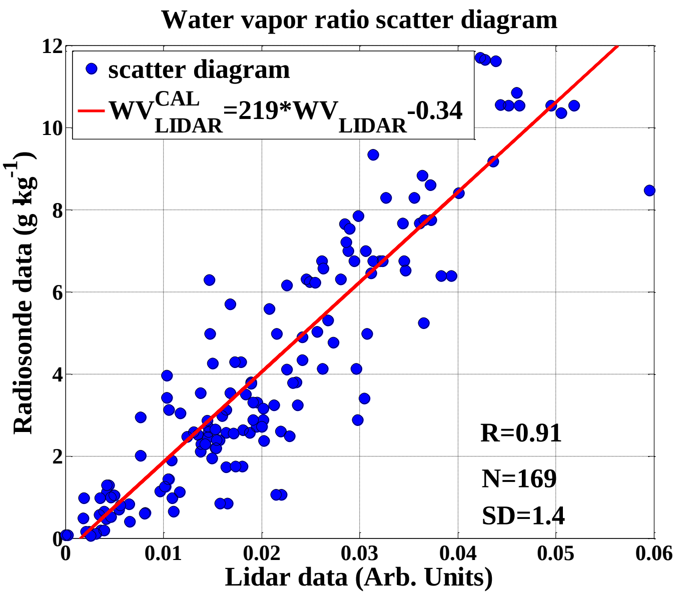

(b)

Fig.2 (a). Distance between sites of WACAL and radiosonde; (b). Regression of WACAL mixing ratio profile to radiosonde measurement

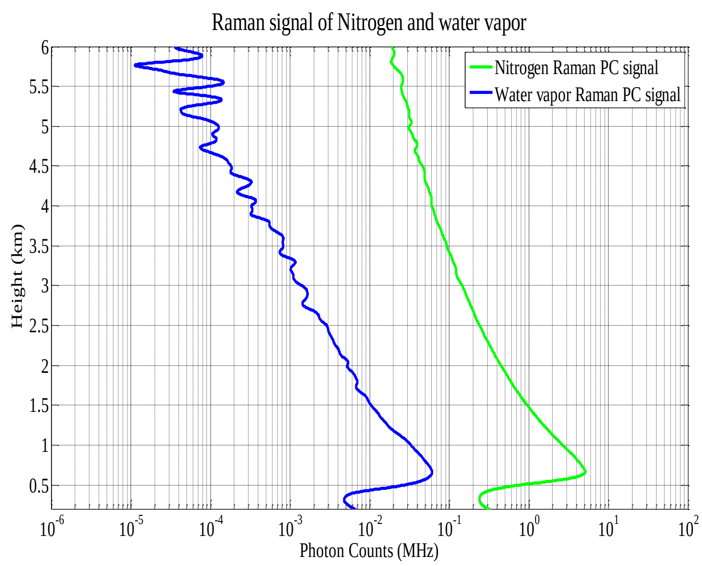

Fig. 3 The actual backscattering signal ~~detected by~~of nitrogen and water vapor Raman channels at night time from 19:00 to 21:00 on 12 June 2014, Qingdao (36.17 °N, 120.5 °E).

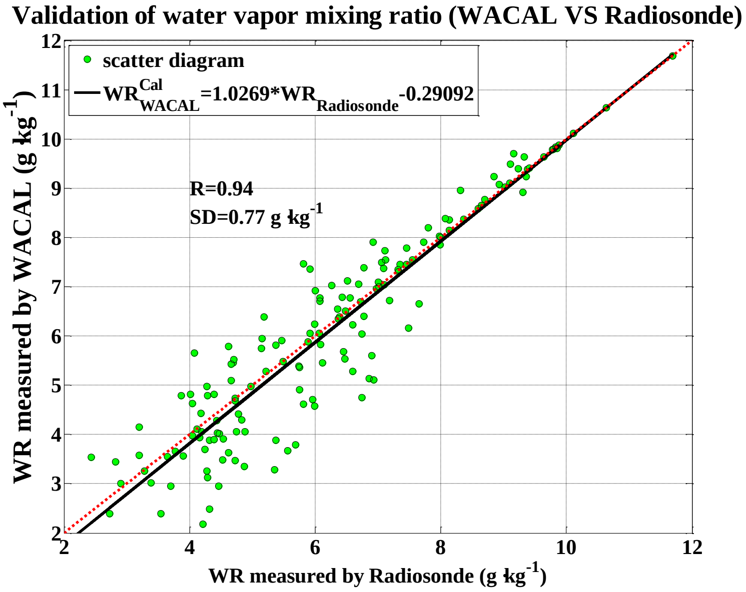

Fig. 4 Validation of the calibrated water vapor mixing ratio (red dashed line is 1:1 curve and black line is fitting curve)

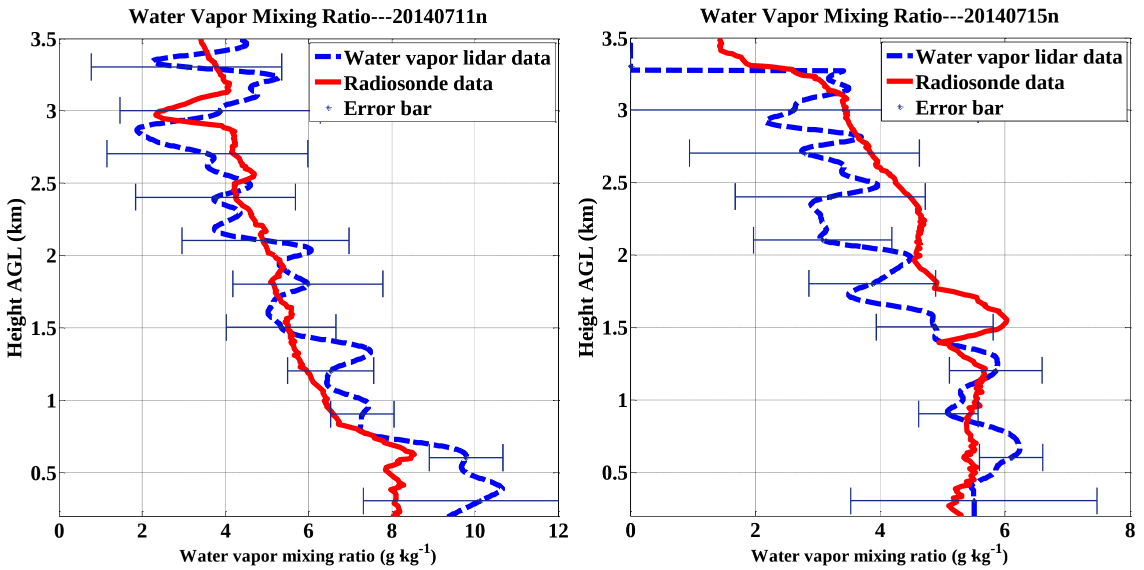

(a) (b)

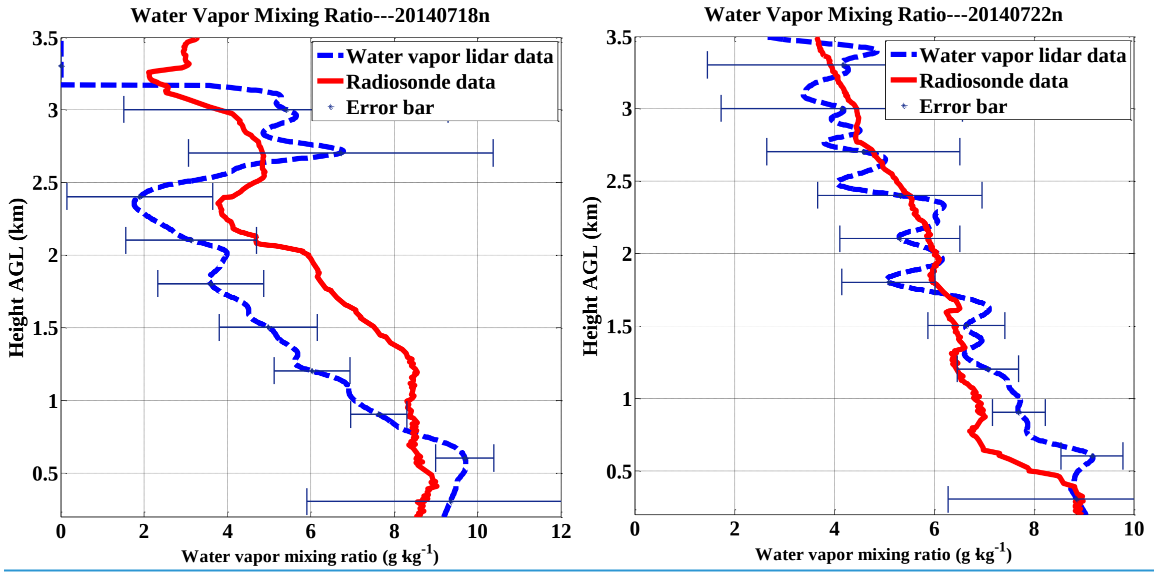

(c) (d)

Fig. 5 Water vapor mixing ratio case studies: (a), (b), (c) and (d) measured in Nagqu on July 11, 15,18 and 22, 2014, respectively.

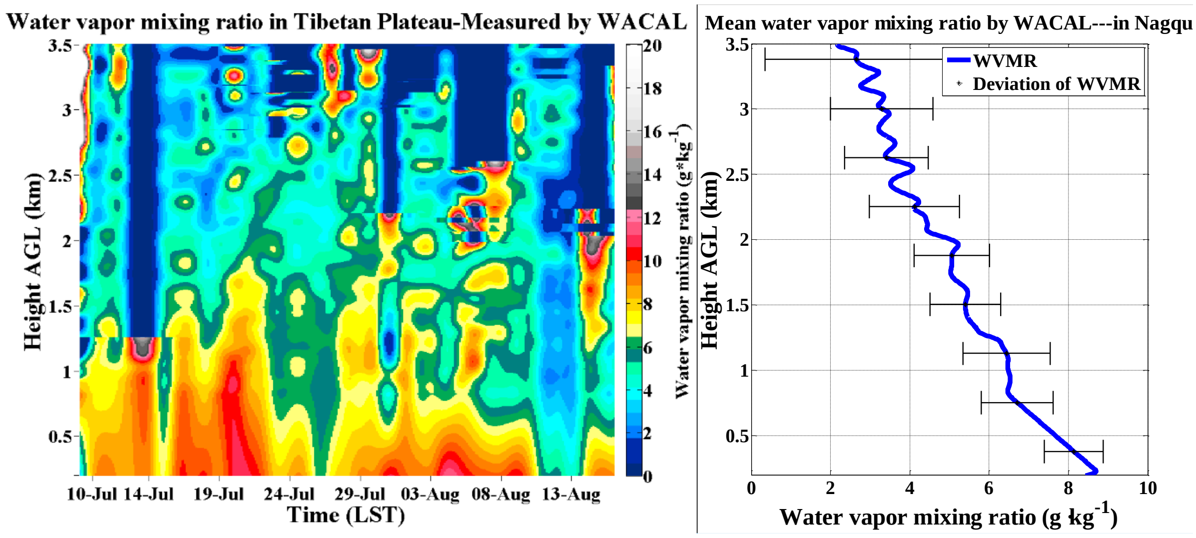

(a) (b)

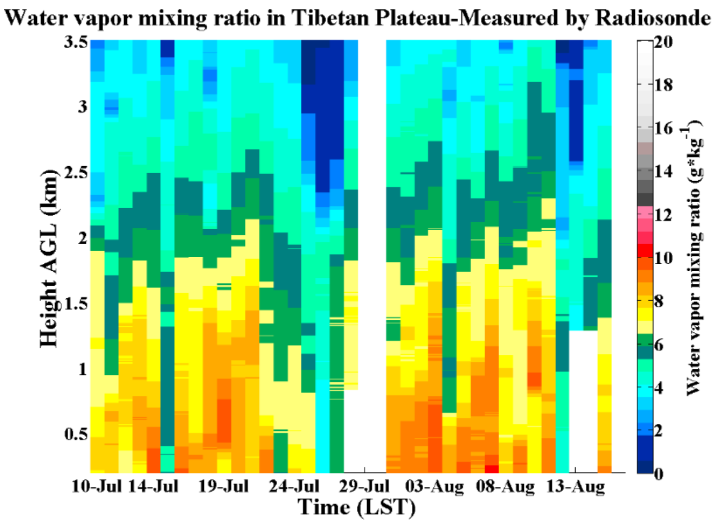

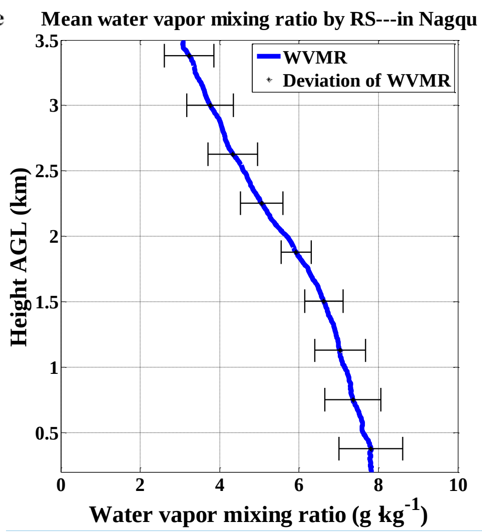

(c) (d)

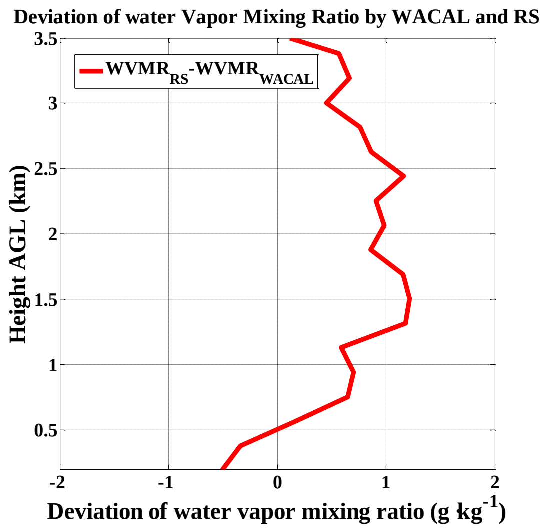

(e)

Fig. 6 ~~Diurnal variation~~(a) Time serials of water vapor mixing ratio at 21:30 LST from 10 July to 16 August measured by WACAL;~~ and~~ (b) Profile of mean water vapor mixing ratio rom 10 July to 16 August measured by WACAL; (c) Time serials of water vapor mixing ratio at 21:30 LST from 10 July to 16 August measured by Radiosonde (RS);~~.~~ (d) Profile of mean water vapor mixing ratio rom 10 July to 16 August measured by RS and (e) Deviation of water vapor mixing ratio measured by WACAL and RS.

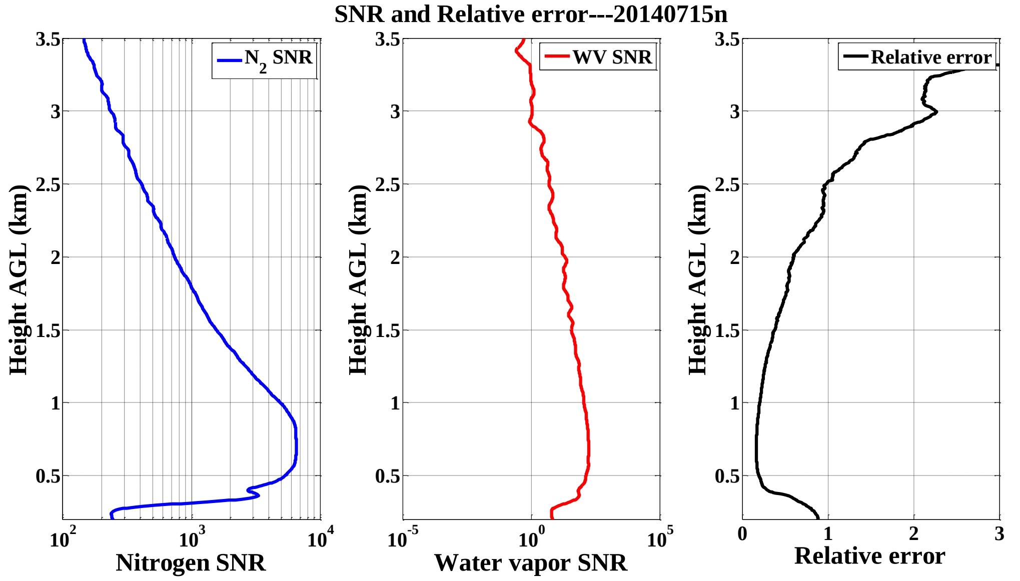

Fig. ~~7~~ 7 The SNR of nitrogen and water vapor Raman signal and the relative error of water vapor mixing ratio at ~~night time~~nighttime of 15 July 2014.

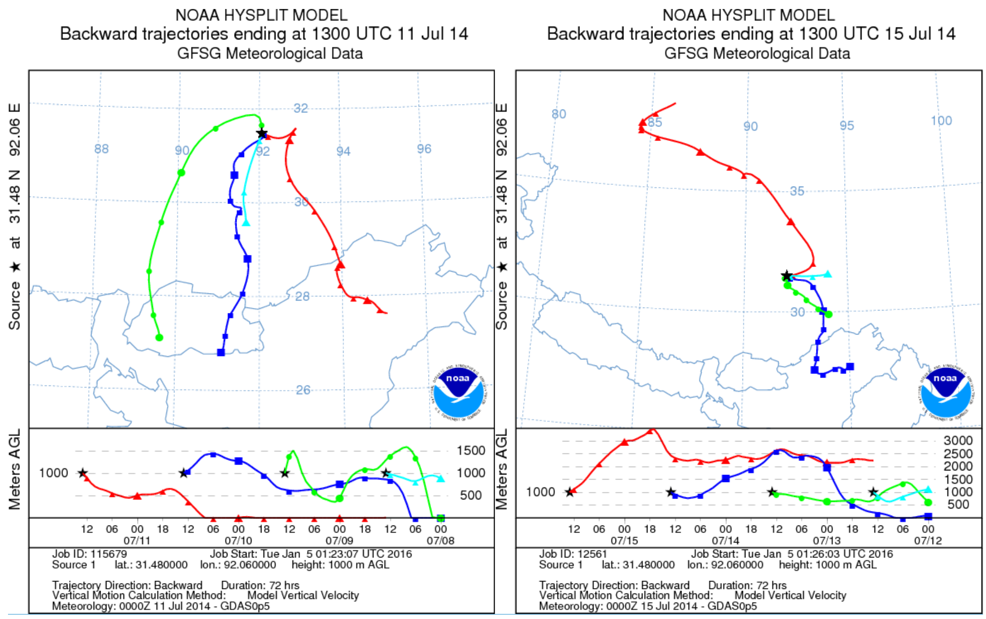

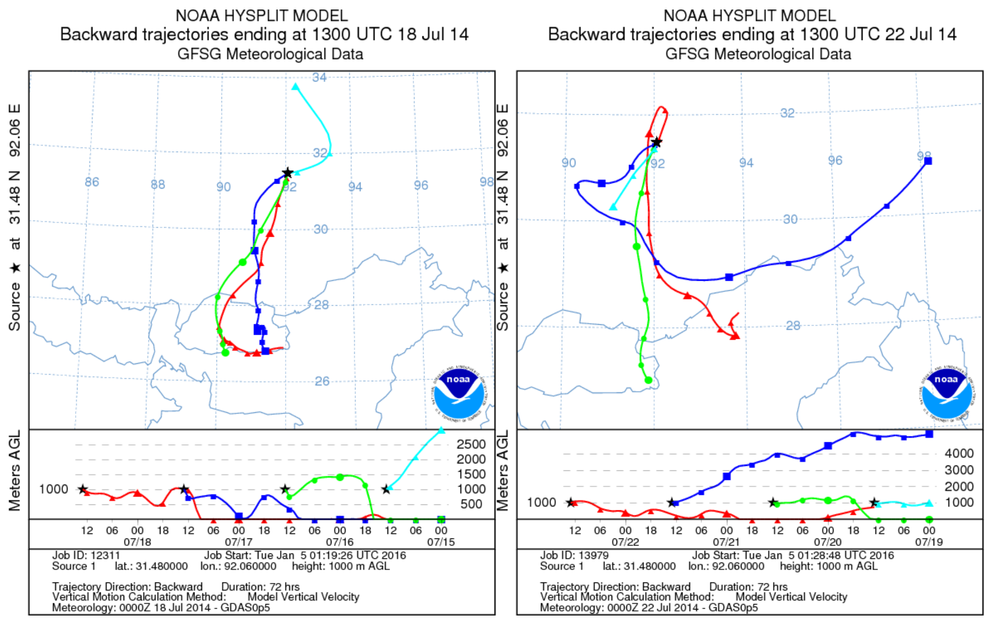

Fig. 8 Backward trajectories ending at 21:00 LST on 11, 15, 18 and 22 July 2014 simulated by HYSPLIT model.

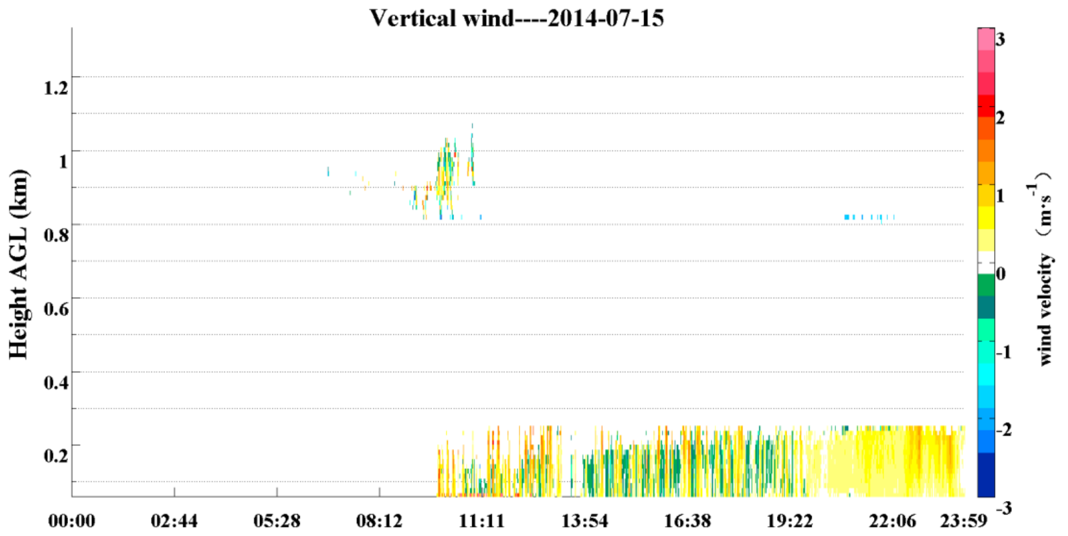

Fig 9. Time serials of vertical wind velocity from 00:00 LST to 23:59 LST, 15 July 2014.

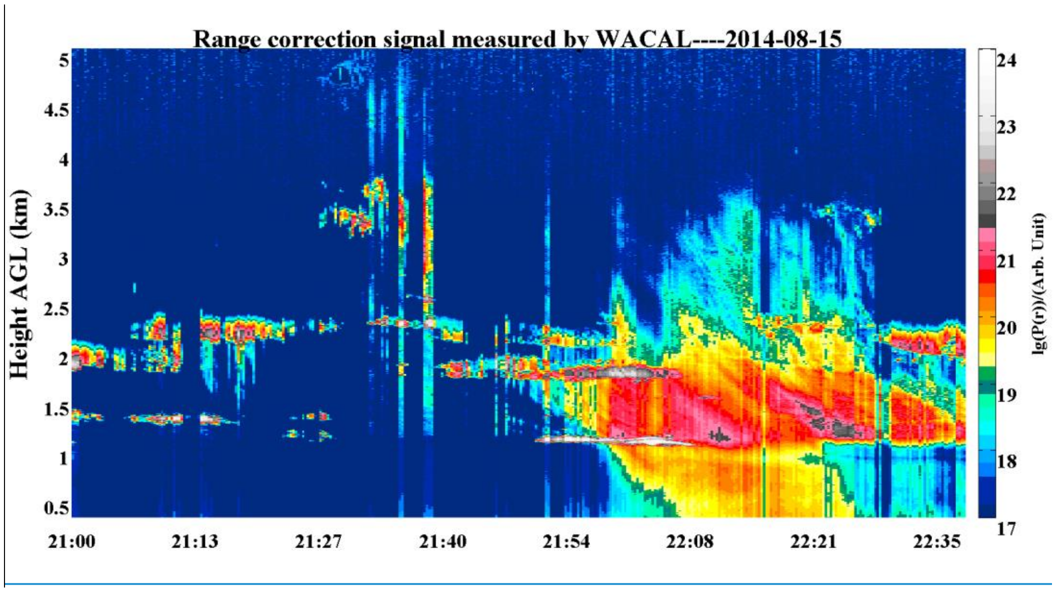
Range correction signal measured by WACAL----2014-08-15
Height AGL (km)
lg(P(r))/(Arb. Unit)
21:00
21:13
21:27
21:40
21:54
22:08
22:21
22:35

(a)

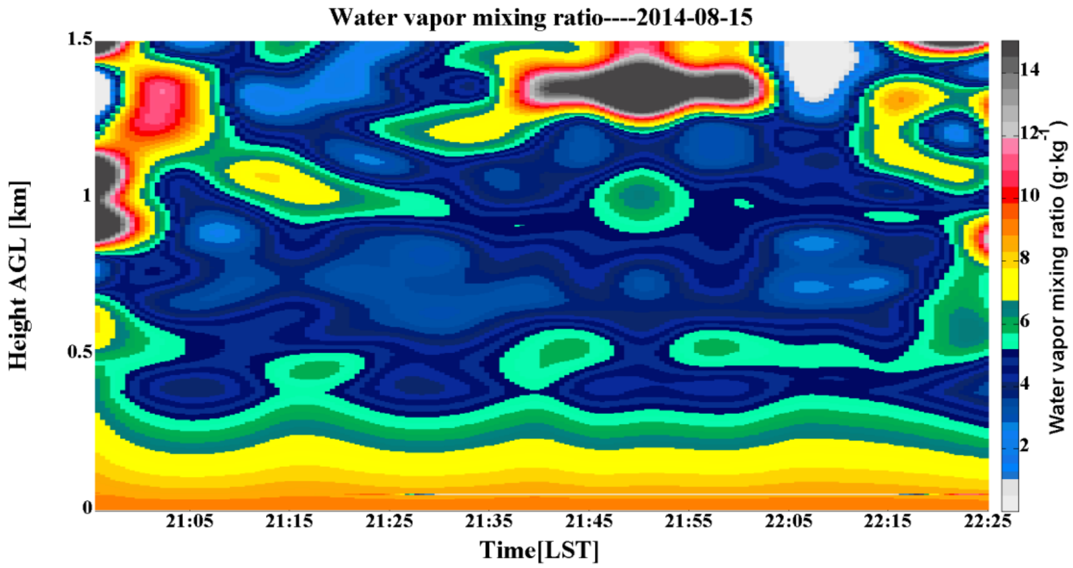
Water vapor mixing ratio----2014-08-15
Height AGL [km]
Time[LST]
Water vapor mixing ratio (g·kg⁻¹)
21:05
21:15
21:25
21:35
21:45
21:55
22:05
22:15
22:25

(b)

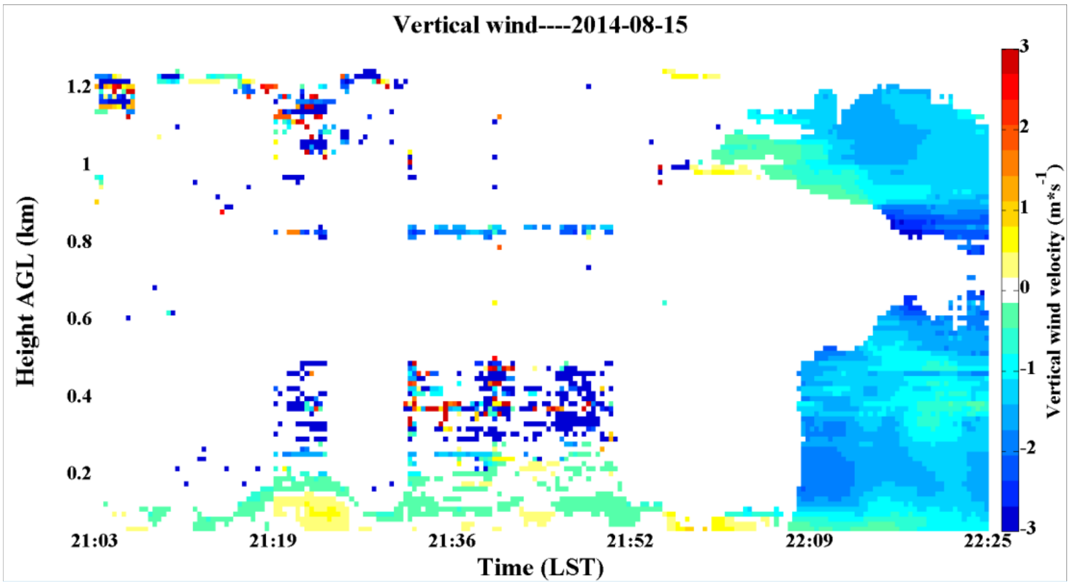

(c)

Fig.~~8~~ **10** (a). Time serials of range correction signal measured by WACAL from 21:00 LST to 22:35 LST;

(b). Time serials of water vapor mixing ratio measured by WACAL from 21:00 LST to 22:25 LST; and~~.~~

(c). Time serials of vertical velocity profile from 21:03 LST to 22:30 LST

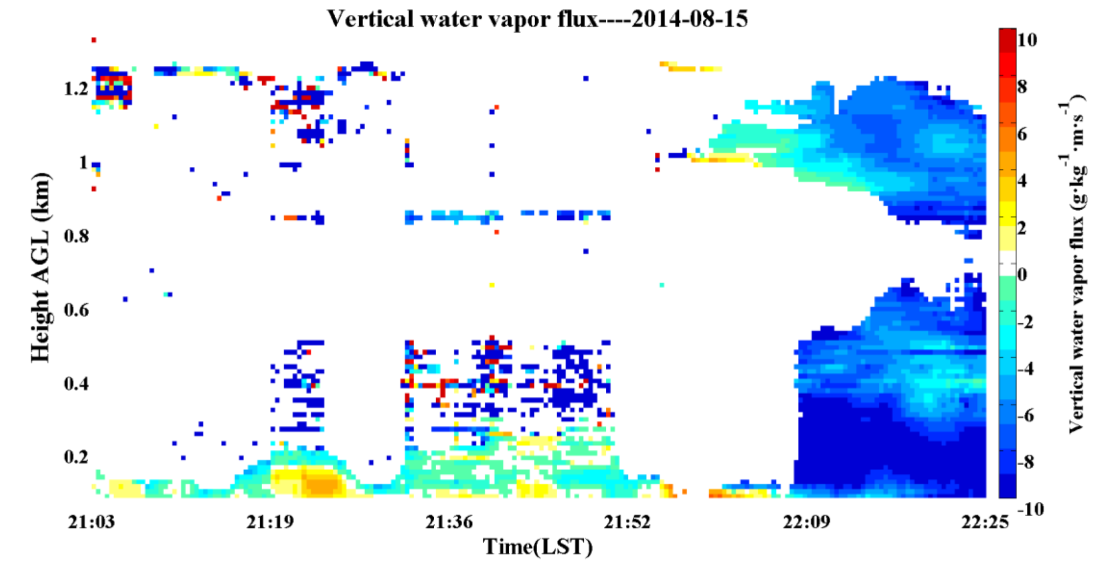

Fig. 11~~9~~ Time serials of vertical water vapor flux from 21:03 LST to 22:30 LST.